Structural evolution and coexistence of ferroelectricity and antiferromagnetism in Fe, Nb co-doped $BaTiO_3$ ceramics

Zimeng Hu[a], *Vladimir Koval*[b], *Yajun Yue*[c], *Man Zhang*[a], *Chenglong Jia*[d*], *Isaac Abrahams*[c*], *Haixue Yan*[a*]

[a] *School of Engineering and Materials Science, Queen Mary University of London, Mile End Road, London E1 4NS, United Kingdom*

[b] *Institute of Materials Research, Slovak Academy of Sciences, Kosice 04001, Slovakia*

[c] *Department of Chemistry, Queen Mary University of London, Mile End Road, London E1 4NS, United Kingdom*

[d] *Key Laboratory for Magnetism and Magnetic Materials of MOE* and Lanzhou Centre for Theoretical Physics, *Lanzhou University*, *Lanzhou 730000, P. R. China*

[*] *Corresponding Authors,*

C. Jia: cljia@lzu.edu.cn

I. Abrahams: i.abrahams@qmul.ac.uk

H. Yan: h.x.yan@qmul.ac.uk

Abstract

Multiferroics are materials that exhibit two or more primary ferroic properties within the same phase and have potential applications in sensors, spintronics and memory devices. Here, the dielectric, ferroelectric and magnetic properties of novel multiferroics derived from $BaTi_{1-x}(Fe_{0.5}Nb_{0.5})_xO_3$ (BTFN, $0.01 \leq x \leq 0.10$) ceramics are investigated. Multiferroism in these ceramics is manifested by the coexistence of ferroelectric long-range ordering and antiferromagnetism. With increasing *x*-value, there is a structural evolution from a tetragonal perovskite to a mixture of tetragonal and cubic phases, accompanied by a decrease in the temperature of maximum permittivity. At room temperature, ferroelectric behaviour is evidenced by the presence of current peaks corresponding to domain switching in the current-electric field loops, while the observation of non-linear narrow magnetic hysteresis loops suggests dilute magnetism. The results indicate that in the $x = 0.07$ composition the antiferromagnetic order is established through an indirect super-exchange interaction between adjacent Fe ions.

Keywords: dielectric, ferroelectric, antiferromagnetic, multiferroics, barium titanium iron niobium oxide.

1. Introduction

The concept of multiferroic materials or multiferroics (MFs) was introduced in 1994 by Schmid [1]. MFs are materials that possess two or more ferroic orders, for instance (anti)ferroelectricity and (anti)ferromagnetism within the same phase. Another functionality in some magneto- and electro-active MFs is introduced by the so-called magnetoelectric (ME) effect, which describes an effective coupling between magnetisation and electrical polarisation. Among MFs, single-phase materials have gained great attention due to their relatively high ME coefficients, offering huge potential for applications in electronic devices, including sensors and four-state logic memories [2]. The two most-studied single-phase MFs are bismuth ferrite ($BiFeO_3$) and terbium manganate ($TbMnO_3$). While the former possesses a high ferroelectric Curie point, T_C (~ 828 °C), and a high Neél magnetic transition temperature T_N (~368 °C) [3], $TbMnO_3$ exhibits a larger ME coefficient than $BiFeO_3$ [4]. Recently, several new types of multiferroic systems with ME coupling have been reported, including (i) charge-frustrated $LuFe_2O_4$ [5], (ii) hexagonal ferrites with conical structure spins, like the Y-type hexaferrite $Ba_2Mg_2Fe_{12}O_{22}$ [6, 7], (iii) $Ba_2CoGe_2O_7$ with p-d hybridisation-induced magnetoelectricity [8], and (iv) metal-organic frameworks with oriented hydrogen bonds [9]. The main drawbacks of these new MFs are: (i) small magnetic moments and low coupling coefficients in the case of Type-I multiferroics, such as $BiFeO_3$, where polarisation and magnetism have different origins and (ii) the existence of ferroelectricity only at very low temperatures in Type-II multiferroics (e.g., $TbMnO_3$), where a particular magnetic structure gives rise to the spontaneous polarisation. These and other usually impurity-related shortcomings [10] have impeded full commercialisation of MFs. Therefore, the development of new single-phase materials exhibiting multiferroic properties at near ambient temperatures is seen as an important objective in addressing issues associated with the miniaturisation of electronic devices.

It has been demonstrated that partial substitution of ions in the A and/or B sites of ABO_3-type perovskite oxides is an effective way of tuning the properties of perovskite-derived MFs [11-14].

Early studies showed that magnetoelectric Type-I MFs can be prepared from Aurivillius phase ferroelectrics by using magnetic ions as dopants (e.g., Fe^{3+}, Mn^{2+}, Mn^{4+} and Co^{3+}) [15-17]. $BaTiO_3$ (BT) is a well-known lead-free ferroelectric material, which exists in one of four perovskite-based polymorphs, depending on temperature, viz.: cubic, tetragonal, orthorhombic and rhombohedral when cooled through the Curie temperature (T_C ~ 120 °C) down to the cryogenic region [18]. At T_C, a ferroelectric phase transition from cubic (*Pm*3*m*) to tetragonal (*P*4*mm*) structures occurs. In the tetragonal phase, the spontaneous polarisation is directed along the *c*-axis, which can be explained within the displacive model by the collective movement of the Ti^{4+} ions in the *c*-axis direction [19, 20].

In 2001, the results of total energy calculations by Nakayama and Katayama-Yoshida [21] suggested that $BaTiO_3$ solid solutions based on doping with transition metals such as Fe, Co, Ni, Cu, Zn, *etc*. may show weak magnetism at room temperature. It was later shown that Fe-, Co-, Mn- and Ni- substituted $BaTiO_3$ bulk samples did indeed exhibit ferromagnetism at room temperature [22-25]. However, the weak ferromagnetic moment of the Fe-doped $BaTiO_3$ ceramics is not an intrinsic property of the main tetragonal phase, but results from the presence of a hexagonal secondary phase [22, 25, 26]. The presence of the secondary phase and structural variations are governed by the oxygen vacancy content which is linked to the extent of doping by the trivalent Fe^{3+} ions [27, 28]. First principles calculations indicated that Fe^{3+} ions occupy different Ti^{4+} sites in the hexagonal phase, Ti(1) (corner-sharing oxygen octahedra) and Ti(2) (face-sharing octahedra), depending on the Fermi energy (E_F) [22]. Interactions between $Fe_{Ti(1)}$ and $Fe_{Ti(1)}$ and $Fe_{Ti(1)}$ and $Fe_{Ti(2)}$ give rise to paramagnetism, while the interaction between $Fe_{Ti(2)}$ and $Fe_{Ti(2)}$ generates antiferromagnetic order [22].

The paraelectric hexagonal phase can be suppressed by the simultaneous doping of a donor dopant and Fe ions in $BaTiO_3$ [29]. Choudhury *et al*. [30] reported that the hexagonal phase in $BaTi_{0.9}Fe_{0.1}O_3$ is destabilised by donor Bi^{3+} doping at the Ba^{2+} site and disappears when the amount of Bi^{3+} is close to 10%. Du *et al*. [31] reported that the formation of the hexagonal phase promoted by acceptor (Fe^{3+}) doping in $Ba(Ti_{0.9}Fe_{0.1})O_3$ can be suppressed by Nb^{5+} donor doping. The hexagonal

phase was found to disappear when the donor content reached 8 mol%, nearly the same concentration as that of the Fe^{3+} ions. Similarly, Das *et al*. [32] reported that equal co-substitution of BT by a magnetic acceptor and a non-magnetic donor can suppress the formation of the hexagonal phase, whilst allowing for the tuning of electrical properties.

Here, we systematically investigate the multiferroic behaviour of $BaTiO_3$ ceramics, equally co-substituted on the B-site by Fe^{3+} and Nb^{5+}, as a function of composition. Fe^{3+} is selected to establish long-range magnetic order, while Nb^{5+} ions are used to charge balance the system to maintain the oxygen stoichiometry and hence inhibit the formation of the hexagonal phase. Equal co-substitution by Fe^{3+} and Nb^{5+} ions has previously been used to alter the diamagnetic behaviour of ferroelectric $PbTiO_3$, [33]. The fully substituted system, $Pb(Fe_{1/2}Nb_{1/2})O_3$, showed ferroelectric and magnetic properties at room temperature [33]. A similar approach is used here to investigate the effect of Fe^{3+}/Nb^{5+} equal co-substitution on the crystal structure, microstructure, dielectric, ferroelectric and magnetic properties of BT with the aim of preparing a single-phase multiferroic ceramic based on a simple perovskite-structured ferroelectric.

2. Materials and methods

$BaTi_{1-x}(Fe_{0.5}Nb_{0.5})_xO_3$ (x = 0.01, 0.03, 0.05, 0.07 and 0.10, abbreviated hereafter as BTFN1, 3, 5, 7 and 10, respectively) ceramics were synthesised by a conventional solid-state method. High purity $BaCO_3$ (Alfa 99.8%), TiO_2 (Aldrich 99.8%), Fe_2O_3 (Alfa 99.945%), and Nb_2O_5 (Alfa 99.9%) powders were used as raw materials and pre-heated at 200 °C for 24 h. Stoichiometric amounts of the raw materials were ball-milled for 6 h in a nylon jar filled with zirconia balls and ethanol using a planetary mill (P5 model IV, Nanjing Machine Factory, China). After drying, the slurry was calcined at 1100 °C in a muffle furnace (Lenton, UK) for 6 h, followed by secondary ball-milling for 6 h to obtain a fine particle size. After sieving the powder (500 μm), 5 wt% of polyvinyl alcohol (PVA) was added and the mixture pressed into disks (13 mm in diameter and 1-2 mm in thickness) at a pressure

of 100 MPa. The pellets were heated at a rate of 10 °C min^{-1} to 650 °C in air and then held at this temperature for 2 h to remove the binder. The sintering temperature was optimised within the temperature range of 1275-1400 °C for each composition based on measurements of sample density. Sintering was carried out at a heating rate of 3 °C min^{-1} with the dwell time at the optimised temperature set to 2 h.

The crystal structure of the sintered $BaTi_{1-x}(Fe_{0.5}Nb_{0.5})_xO_3$ ceramics was investigated by X-ray powder diffraction (XRD, PANalytical, Cubix) on crushed powders using Ni-filtered Cu-Kα radiation (λ = 1.5418 Å) over the 2θ range from 5 to 120°, in steps of 0.0315°, with an effective scan time of 200 s per step using a PIXcel (1D) detector. Rietveld refinement was performed using the GSAS package [34] with the EXPGUI interface [35]. Initial models were based on the tetragonal and cubic structures of $BaTiO_3$ presented by Buttner and Maslen in space groups *P*4*mm* and *Pm*-3*m*, respectively [36]. Surface morphology was analysed using a scanning electron microscope (SEM, FEI Inspect-F, Oxford), with an accelerating voltage of 5 kV. The surface element analysis of BTFN ceramics was performed using an X-ray photoelectron spectrometer (Nexsa, XPS system). Spectral fitting was carried out using a Gaussian-Lorentzian function [37] as implemented in the Avantage software (Thermo Scientific, USA).

For electrical property measurements, the as-sintered pellets were ground to about 0.4 mm thickness, and then coated with silver paint (Gwent Electronic Materials Ltd., C2011004D5, Pontypool, U.K.). The temperature dependencies of the relative dielectric permittivity (ε') and loss tangent (tan δ) were measured over the temperature range -195 °C to 160 °C at various frequencies from 500 Hz to 100 kHz via a computer-controlled system consisting of an LCR meter (Agilent, 4284A, USA) attached to a low-temperature testing chamber. Both the electrical polarisation - electric field (*P*-*E*) and electrical current - electric field (*I*-*E*) loops were measured in silicone oil at room temperature using a ferroelectric tester (NPL, Teddington, U.K.) [38]. The testing frequency of the triangular voltage waveforms was set to 10 Hz. Superconducting quantum interference device

(SQUID (MPMS+VSM), Quantum Design, U.S.A.) magnetometry was employed to collect magnetisation – magnetic field (*M-H*) hysteresis loops at 300 K and 5 K. The temperature dependence of magnetisation was collected at a magnetic field of 1000 Oe applied to samples after zero field cooling (ZFC) and field cooling (FC).

3. Results and discussion

The XRD patterns of the studied $BaTi_{1-x}(Fe_{0.5}Nb_{0.5})_xO_3$ ceramics are shown in Fig. 1a. All samples adopt a perovskite type structure with no detectable impurities. The patterns for the $x = 0.01$ and 0.03 compositions can be readily indexed in the tetragonal space group *P*4*mm* ($a \approx 3.9995$ Å, $c \approx 4.0342$ Å). Close inspection of the diffractograms in Fig. 1b reveals a merging of the (002) and (200) peaks at *ca*. 45° 2θ into a single broad peak as *x* increases from 0.01 to 0.10. To further confirm the structural evolution with composition, Rietveld analysis was performed. The fitted diffraction profiles are presented in Fig. S1, with the crystal and refinement parameters summarised in Table S1. Despite the apparent merging of the (002) and (200) peaks, attempts to fit the data for the $x = 0.05$ sample to a cubic perovskite model in space group *Pm*-3*m* ($a \approx 4.008$ Å) invariably resulted in significantly higher R-factors than the tetragonal model and a negative thermal parameter for the A-site Ba^{2+} cation. A dual-phase model involving a combination of the tetragonal and cubic phases gave a significantly better fit (as determined by the Hamilton F-Test [39]) than a pure tetragonal model. The refined weight fractions indicate the major phase to be tetragonal (96.6(1)%). Similar results were obtained for the $x = 0.07$ composition, while the refinement for the $x = 0.10$ composition shows that the proportion of the secondary cubic phase increases to 20.6(1)% (Fig. S2). Fig. 1c and 1d show the compositional variation of the lattice parameters and unit cell volume, respectively. The tetragonal lattice constants (a_T and c_T) approach each other with increasing dopant concentration up to $x = 0.07$, but the axial ratio (c_T/a_T) never reaches unity. The unit cell volume of the major tetragonal phase shows a general increasing trend up to $x = 0.07$, consistent with the substitution of smaller Ti^{4+} ions (ionic radius, $r = 0.605$ Å) by larger Fe^{3+} ($r = 0.645$ Å) and Nb^{5+} ($r = 0.640$ Å) ions [40], but then

shows a decrease at $x = 0.10$ where significant amounts of the larger volume cubic phase are observed. This decrease in volume is also reflected in both the a_T and c_T lattice parameters and suggests that the tetragonal phase at $x = 0.10$ is richer in Ti than would be expected from the starting composition.

Fig. 2 shows SEM images of the studied $BaTi_{1-x}(Fe_{0.5}Nb_{0.5})_xO_3$ ceramics. All the samples are dense with sintered density values higher than 96% of the theoretical value, as measured by the Archimedes method. The density measurements showed that the optimal sintering temperature depends on the dopant concentration and increases from 1275 °C for BTFN1 to 1400 °C for BTFN10. Upon doping, the average grain size decreases from 10 μm ($x = 0.01$) to about 1 μm ($x = 0.10$). Fe doping is known to suppress grain growth in $BaTiO_3$ [41], and in the present system the decreasing trend in grain size appears to be correlated with increasing Fe^{3+} content.

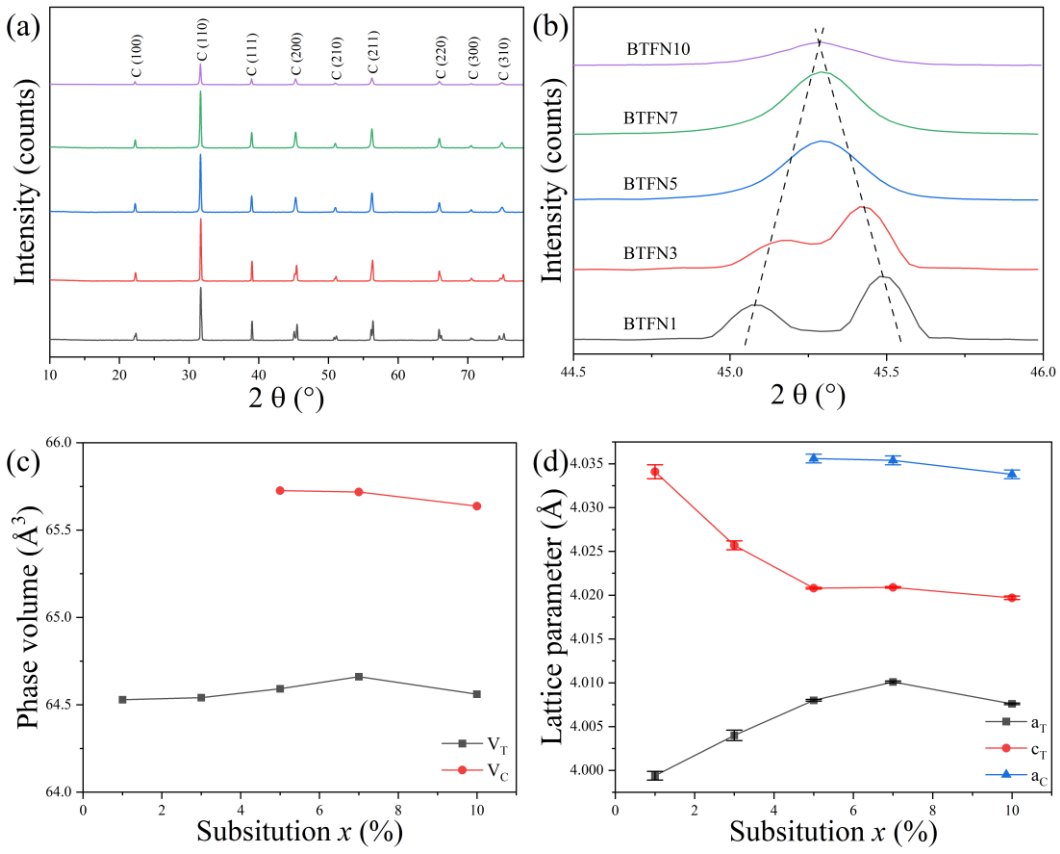

Fig. 1. Structural analysis of $BaTi_{1-x}(Fe_{0.5}Nb_{0.5})_xO_3$ ceramics: (a) XRD patterns of $BaTi_{1-x}(Fe_{0.5}Nb_{0.5})_xO_3$ ceramics; (b) the (200) and (002) diffraction peaks around $2\theta = 45°$; (c) and

(d) compositional evolution of the unit cell volume and lattice parameters, respectively, (Miller indices for the cubic perovskite phase are shown in (a)).

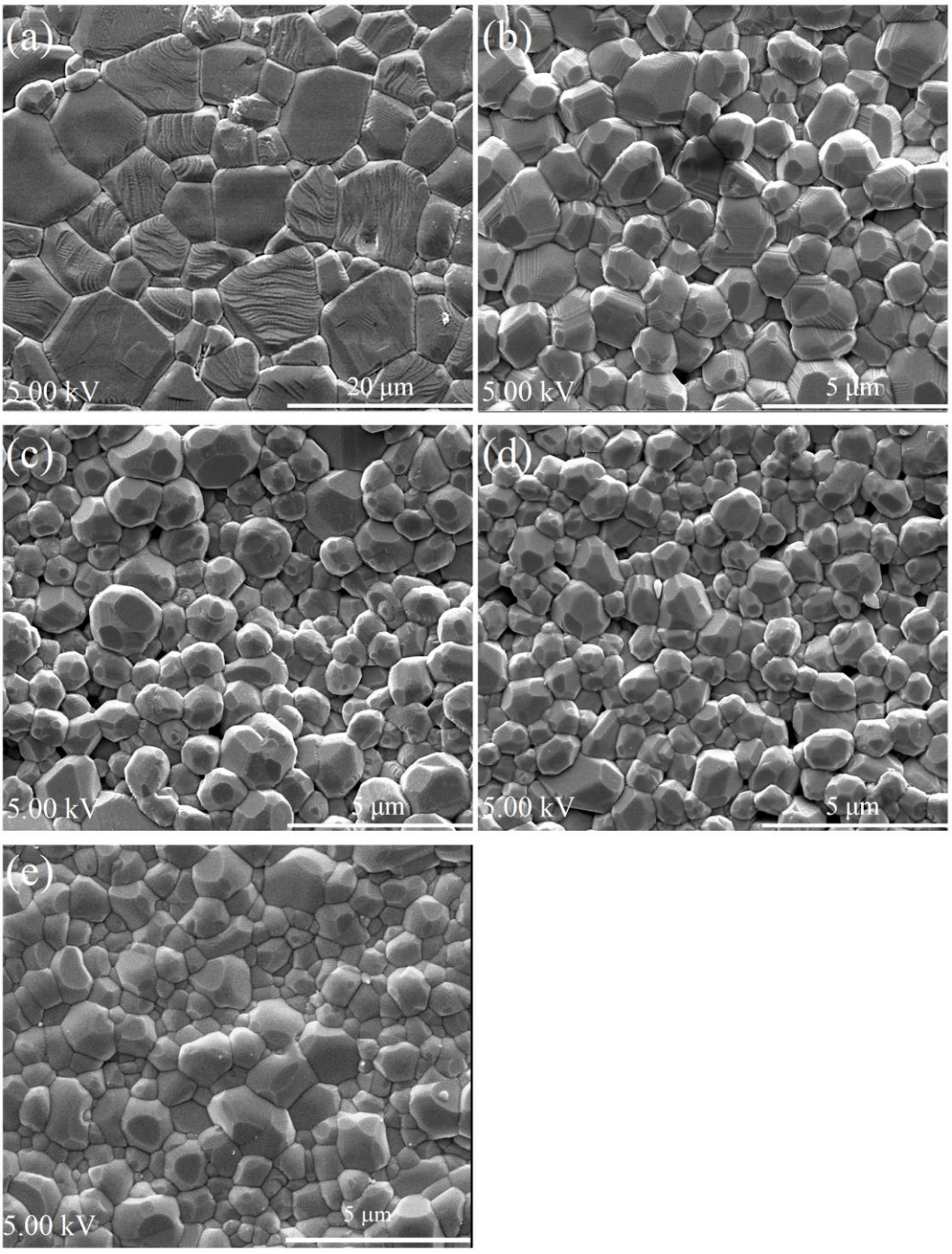

Fig. 2. SEM images of $BaTi_{1-x}(Fe_{0.5}Nb_{0.5})_xO_3$ ceramics: (a) BTFN1, (b) BTFN3, (c) BTFN5, (d) BTFN7, and (e) BTFN10.

Fig S3 shows the fitted Fe 2p XPS spectra for all the studied compositions with fitted parameters given in Table S2. Characteristic Fe $2p_{3/2}$ and $2p_{1/2}$ peaks are observed at about 711 eV

and 724 eV, respectively. Fitting of the data revealed the presence of both Fe^{2+} and Fe^{3+} species. The reduction of Fe^{3+} is common during high temperature sintering [42] and based on the areas of the deconvoluted spectra, the Fe^{2+}:Fe^{3+} ratio varies from 0.09(2) in BTFN1 to 0.40(5) in BTFN10, indicating an increasing degree of reduction with increasing dopant concentration. These large proportions of Fe^{2+} are likely limited to the surface regions as the XRD data show no evidence of significant structural changes or high concentrations of oxygen vacancies which would necessarily accompany such reduction. Nevertheless, some degree of reduction in the bulk may occur and the associated vacancies would be expected to bring about an increase in loss tangent at room temperature. Fig. 3 displays the fitted O 1s XPS spectra of all the studied compositions. The broad O 1s peak can be deconvoluted into three individual peaks. The most intense peak at around 529.5 eV (red line) corresponds to the lattice oxygen (O_{latt}), the second peak at about 531 eV (blue line) can be attributed to oxygen in the vicinity of an oxygen vacancy (O_{vac}), and the last peak at around 532 eV (green line) relates to the chemisorbed oxygen on the sample surface (O_{abs}) [43, 44]. Although O_{vac} does not correspond directly to the oxygen vacancy content, the ratio of integrated areas of O_{vac}:O_{latt} can be used to compare the change in relative oxygen vacancy concentration between compositions. The O_{vac}:O_{latt} area ratio shows an obvious increasing trend from 0.049(4) (x = 0.01) to 0.095(2) (x = 0.10) as plotted in Fig. 3f. Overall, the reduction of Fe^{3+} and existence of O_{vac} species are supportive of oxygen vacancies in the prepared ceramics which can influence the electrical performance of these ferroelectrics. The fitted Nb 3d XPS spectra for all compositions are shown in Fig. S4. Each spectrum shows a characteristic $3d_{5/2}$ (around 207 eV) and $3d_{3/2}$ (around 210 eV) doublet with an energy gap of around 2.8 eV, which is characteristic of Nb is the 5+ oxidation state [45] and shows little compositional variation, as shown in Table S2. The results appear to confirm that the presence of oxygen vacancies is mainly as a result of reduction of Fe^{3+} rather than Nb^{5+}.

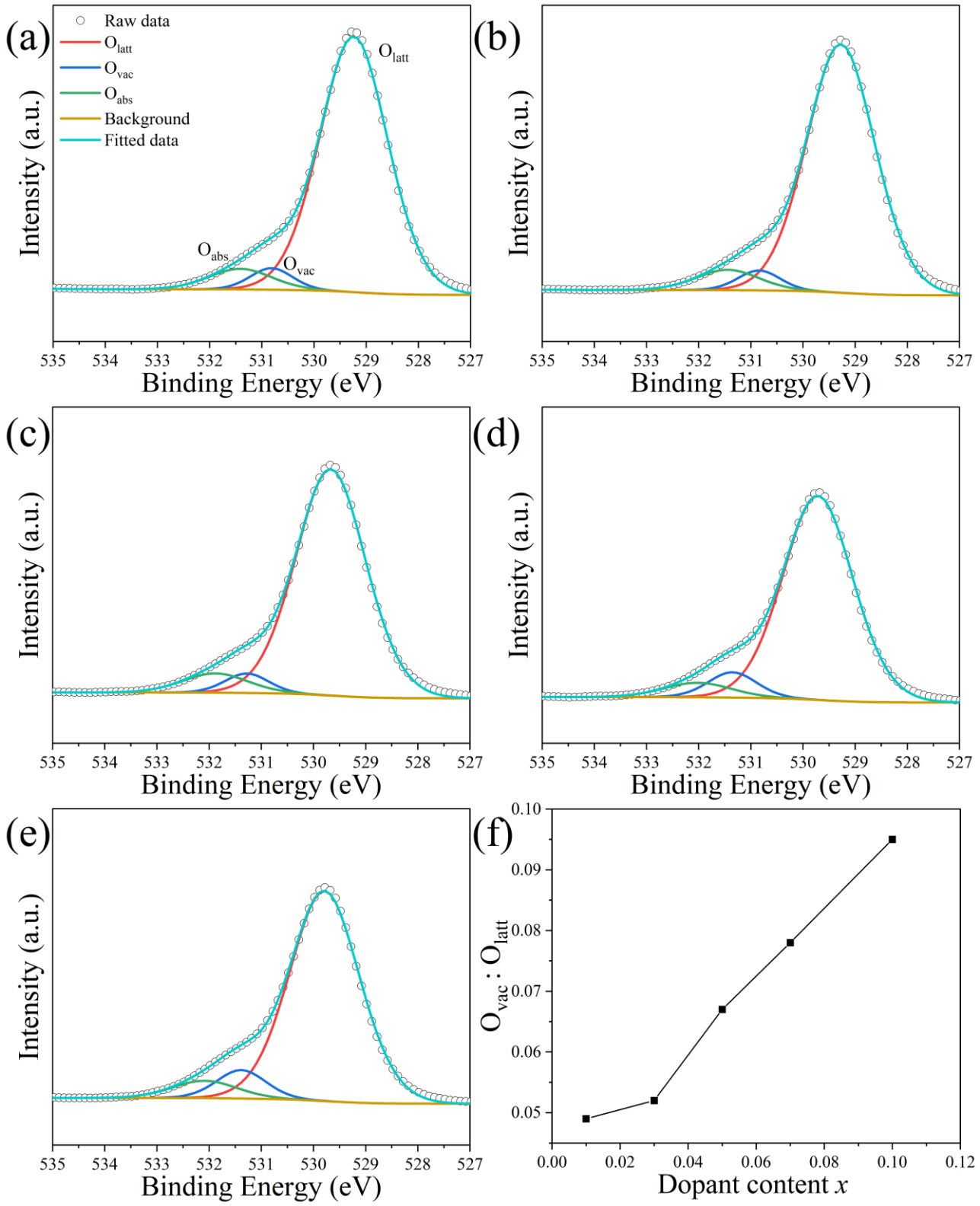

Fig. 3. Fitted O 1s spectra for $BaTi_{1-x}(Fe_{0.5}Nb_{0.5})_xO_3$ compositions: (a) BTFN1, (b) BTFN3, (c) BTFN5, (d) BTFN7 and (e) BTFN10; (f) compositional variation of the O_{vac} : O_{latt} ratio.

The temperature dependencies of relative dielectric permittivity and loss tangent for the studied BTFN compositions are shown in Fig. 4. It is well established that undoped $BaTiO_3$ undergoes three consecutive phase transitions on cooling from high temperature: (i) from non-polar cubic to polar tetragonal (around 120 °C), (ii) from tetragonal to orthorhombic (3 °C), and (iii) from polar orthorhombic to polar rhombohedral (-92 °C). The temperature of the ferroelectric phase transition (the Curie temperature, T_C) is reported to be about 120 °C [46]. The three phase transitions (with the corresponding temperatures labelled as T_m, T_2 and T_3) can clearly be distinguished in BTFN1 and BTFN3 ceramics as local maxima (dielectric peaks) in the permittivity plots and local maxima (loss peaks) in the loss tangent plots in Fig. 4a and 4b. In BTFN5 (Fig. 4c) and BTFN7 (Fig. 4d), the peaks corresponding to the second and third phase transitions approach each other (indicated as $T_2(T_3)$), and, ultimately, for the $x = 0.10$ composition (Fig. 4e), the ceramic shows only one broad peak at T_m. Upon doping, the temperature corresponding to the maximum permittivity (T_m) decreases almost linearly (see Fig. 5a), from 112 °C (for $x = 0.01$) to -35 °C (for $x = 0.10$). The addition of Fe^{3+} and Nb^{5+} ions is believed to promote the stability of the centrosymmetric cubic (Pm-3m) structure at lower temperatures, which is consistent with the XRD analysis, and leads to the observed decrease in T_m. Similarly, the T_2 temperature (at 500 Hz) decreases from around 24 °C (BTFN1) to 16 °C (BTFN3) to 8 °C (BTFN5), as shown in Fig. 5a, revealing that the temperatures of the phase transitions from tetragonal to orthorhombic and from orthorhombic to rhombohedral phases get closer to each other on doping. It should be noted that the value of T_m in all compositions, except $x = 0.10$, is higher than room temperature, implying that they possess ferroelectric properties at ambient temperature. The BTFN1 composition exhibits the highest value of dielectric permittivity (~ 9000), which decreases with increasing dopant concentration. When the frequency increases, ε' is seen to decrease, most likely because some dipoles cannot easily be switched at high frequency. For all the compositions, dielectric loss peaks can be observed below T_m due to domain wall movements. With increasing dopant concentration, the loss tangent at room temperature slightly increases especially for BTFN7

and BTFN10. These two compositions show the largest values of tan δ among the studied samples, due to the proximity of their T_m values to room temperature.

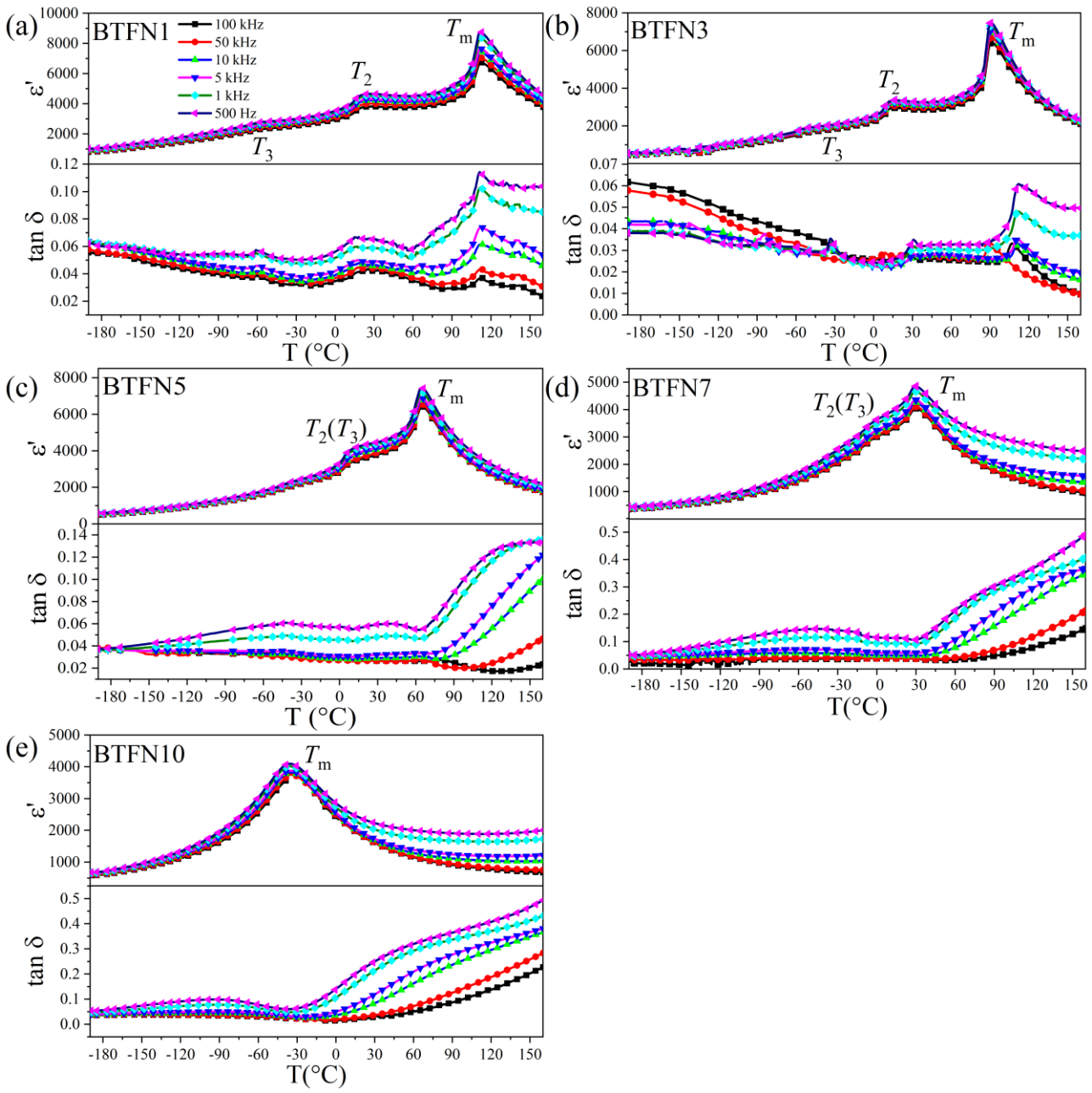

Fig. 4. Temperature dependencies of ε′ and tan δ in $BaTi_{1-x}(Fe_{0.5}Nb_{0.5})_xO_3$ compositions: (a) BTFN1, (b) BTFN3, (c) BTFN5, (d) BTFN7 and (e) BTFN10 ceramics measured at selected frequencies in the range of 500 Hz - 100 kHz.

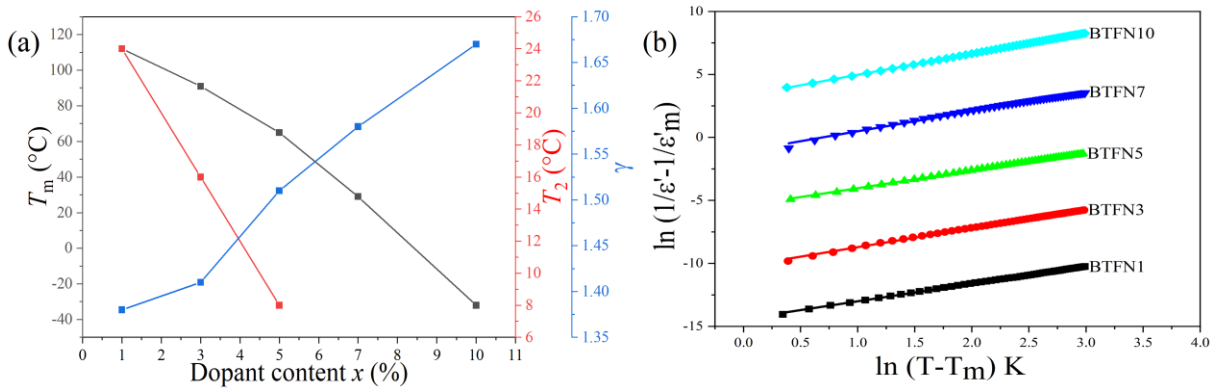

Fig. 5. (a) Compositional dependencies of the temperature of maximum permittivity (T_m), T_2 corresponding to the second anomaly, and the degree of diffusion (γ); (b) plots of ln ($1/\varepsilon'-1/\varepsilon'_m$) versus ln ($T-T_m$) for BTFN ceramics at 500 Hz; solid lines are fits based on the modified Curie-Weiss law.

A diffuse phase transition (a broad dielectric peak) and a frequency-dependent maximum of ε' (ε'_m), typical features of substitutionally modified ABO_3-type ferroelectrics [47-49], are observed for all BTFN compositions. The broader phase transition peak occurs in the solid solution system as a consequence of the random distribution of Fe and Nb cations on the B sites. For a better understanding of these diffuse phase transitions, a modified Curie-Weiss law was used to fit the data above T_m [50]. The relationship between the inverse dielectric permittivity and temperature above T_m can be expressed as follows:

$$\frac{1}{\varepsilon'} = \frac{1}{\varepsilon'_m} + \frac{(T - T_m)^\gamma}{C}$$

where ε'_m, is the maximum permittivity, C is the Curie-Weiss constant and γ is a coefficient which describes the degree of diffusion. For a conventional ferroelectric, the mean value of γ is 1, while for an ideal relaxor ferroelectric $\gamma = 2$. The value of γ for a single-site doped ferroelectric is usually between 1 and 2. The Curie-Weiss fits for the BTFN ceramics are shown in Fig. 5b. Upon doping, the calculated γ-coefficient increases from 1.39(5) (for $x = 0.01$) to 1.67(2) (for $x = 0.10$), as presented in Fig. 5a, indicating that the doping enhances the diffuse nature of the transition in BTFN ceramics.

The random occupation of the dopants on the B site causes local polar structures in the average perovskite structure and has been reported in other transition metal-doped perovskite ceramics [51]. The Curie-Weiss constant (C) of BTFN ceramics is about 10^5 to 10^6 which is similar to that of undoped $BaTiO_3$ (10^5) [52]. The ferroelectric polarisation can be related to the cooperative displacement of cations in the BTFN perovskite. A high value of C (*ca*. 10^6) was found in BTFN10 due to the enhanced diffuse phase transition.

Fig. 6 shows the ferroelectric *P*-*E* and *I*-*E* hysteresis curves of the BTFN ceramics. From the figure, it can be seen that at room temperature all the compositions, except BTFN10, exhibit ferroelectric behaviour, manifested by the occurrence of current peaks in the *I*-*E* loops corresponding to domain switching (Fig. 6b) [53]. Due to its high conductivity and low T_m (below room temperature), ferroelectric domain switching in BTFN10 could not be induced even at high electric fields. The remanent polarisation and maximum polarisation (P_r and P_m) substantially decreased as the dopant content (x) increased. Analogous behaviour can be seen for the coercive field (E_c) in Fig. 6c. Usually, lossy *P*-*E* loops are linked to the oxygen vacancies created by the dopants in $BaTiO_3$ based ceramics [54]. In this respect, the high dielectric loss in the compositions x = 0.07 and 0.10 are believed to originate from the increased vacancy concentration caused by the greater susceptibility of Fe^{3+} to reduction, as evidenced in the XPS data.

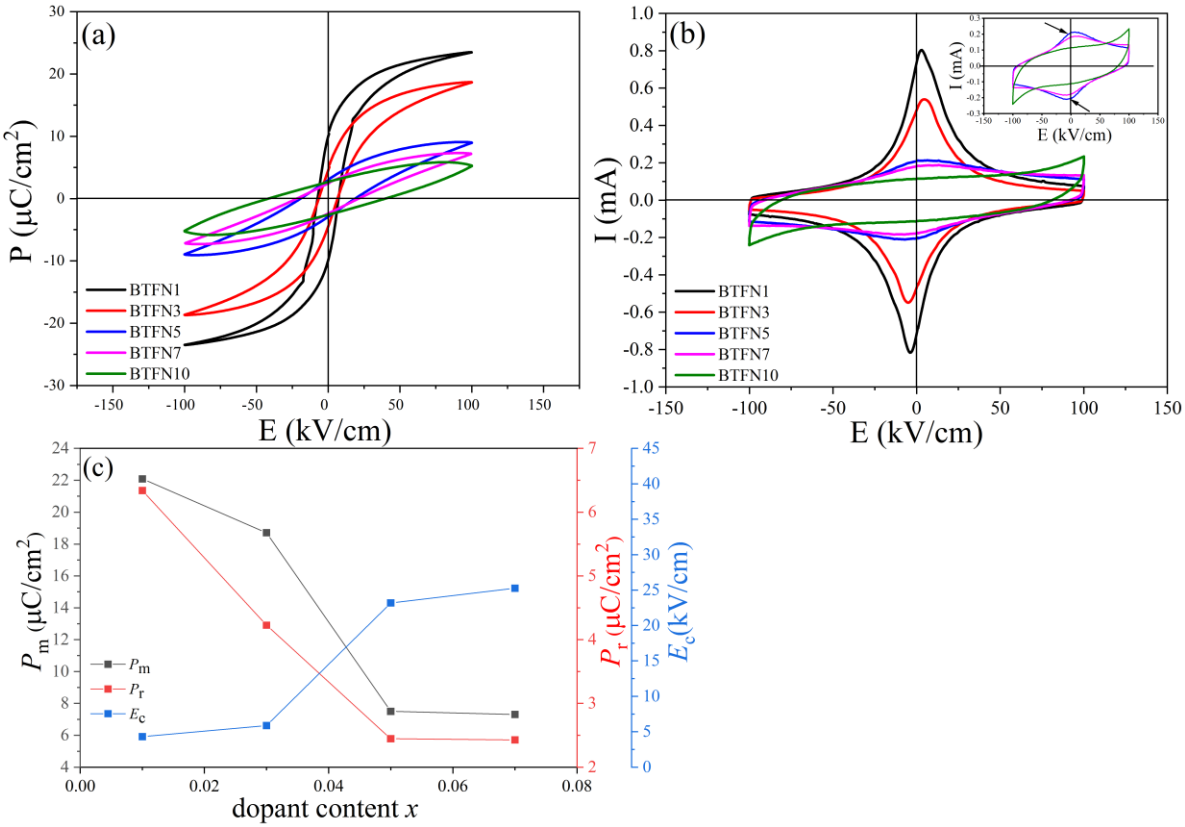

Fig. 6. Ferroelectric *P-E* (a) and *I-E* (b) hysteresis loops of $BaTi_{1-x}(Fe_{0.5}Nb_{0.5})_xO_3$ ceramics, as recorded at room temperature and 10 Hz; (c) ferroelectric characteristics (P_m, P_r, and E_c) in $BaTi_{1-x}(Fe_{0.5}Nb_{0.5})_xO_3$ ($0.01 \leq x \leq 0.07$) ceramics as functions of dopant content (x).

SQUID magnetometry was employed to investigate the magnetic properties of the Fe and Nb co-doped $BaTiO_3$ ceramics. Fig. 7a shows the magnetisation versus magnetic field (*M-H*) hysteresis loops of the ceramic samples, as collected at 5 K. Magnetisation as a function of temperature for the BTFN ceramics subjected to an external magnetic field of 1000 Oe after zero field cooling (ZFC) and field cooling (FC) are presented in Fig. 7b, with *M-H* loops at room temperature shown in Fig. S5. Macroscopically, all the samples are paramagnetic at room temperature, which is manifested by the roughly linear *M-H* loops (shown in Fig. S5) and monotonously decreasing trend in ZFC/FC magnetisation curves (Fig. 7b). However, *M-H* hysteresis observed at 5 K implies an indirect magnetic exchange interaction between the Fe ions in local regions of BTFN. The temperature

dependence of the reciprocal of magnetic susceptibility ($1/\chi$) for the x = 0.07 sample is displayed in the inset of Fig. 7b. The $1/\chi$ data were fitted using the Curie Weiss law [55]:

$$\chi = \frac{C}{T-\theta_{CW}}$$

where C is the Curie constant and θ_{CW} is the Curie-Weiss temperature. The value of θ_{CW} for the x = 0.07 composition is negative (θ_{CW} = -3.80 K), indicating that at very low temperatures there exists locally weak antiferromagnetic ordering in the BTFN7 sample [56]. The coincidence of the non-linear *M-H* loops of the BTFN7 and BTFN10 samples suggests that the short-range antiferromagnetic order is developed locally also in Fe-rich regions of the $x = 0.10$ samples. According to the Goodenough rules [57], the antiferromagnetic behaviour can be explained by super-exchange interactions of the type Fe^{3+} -O^{2-}- Fe^{3+}. It is anticipated that antiferromagnetic order can be achieved in transition metal doped $BaTiO_3$ by increasing the concentration of spins. Such an approach would lead to the design of novel functional multiferroics via chemical modification of well-established ferroelectrics using magnetic ions.

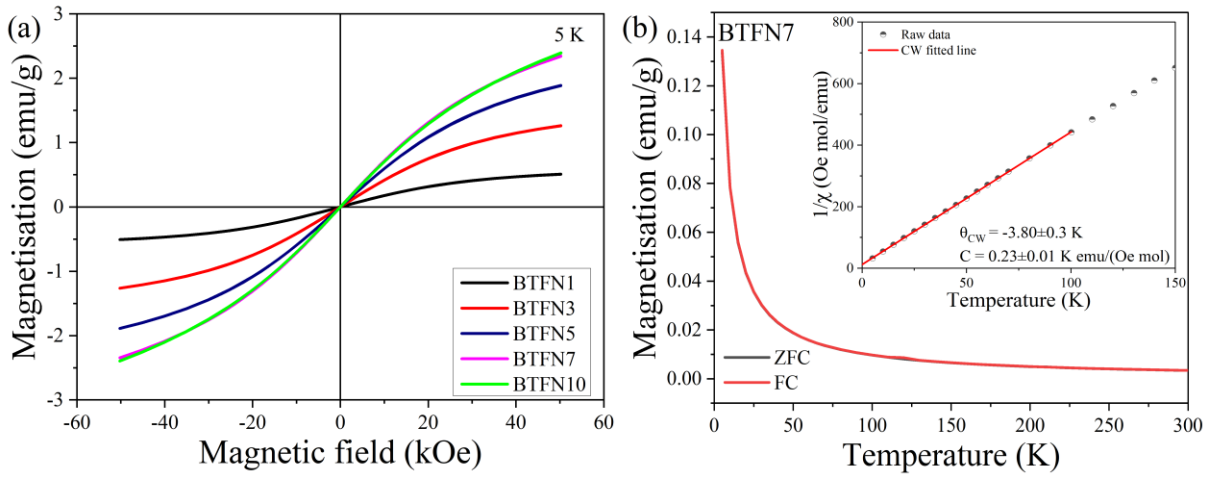

Fig. 7. (a) *M-H* loops of $BaTi_{1-x}(Fe_{0.5}Nb_{0.5})_xO_3$ ceramics at 5 K and (b) ZFC and FC magnetisation curves for the x = 0.07 composition under an external magnetic field of 1000 Oe. The inset shows

the fitted reciprocal magnetic susceptibility as a function of temperature (fitting to the Curie-Weiss law).

4. Conclusions

$BaTi_{1-x}(Fe_{0.5}Nb_{0.5})_xO_3$ ($0.01 \leq x \leq 0.10$) ceramics were prepared by a conventional solid-state reaction method. The room-temperature XRD patterns revealed a composition-driven transformation of the crystal structure from a pure tetragonal *P*4*mm* phase to a mixture of cubic *Pm*-3*m* and *P*4*mm* phases with increasing *x*-value. The temperature of maximum dielectric permittivity, T_m, was found to decrease with increasing dopant content, which is consistent with the structural evolution from a strong polar phase to a weak polar phase at room temperature. The domain switching, observed in the room temperature *P*-*E* and *I*-*E* hysteresis loops of the ceramics with low dopant concentrations, reflects the ferroelectric nature of the samples. From the magnetisation hysteresis loops, it is suggested that all the samples are paramagnets at room temperature. The paramagnetic behaviour can be attributed to the low concentration of Fe^{3+} ions which are randomly distributed over perovskite B sites. Antiferromagnetic order is proposed to occur locally in Fe-rich regions of the $x = 0.07$ and 0.10 ceramics, which is indicative of a multiferroic state in these two compositions.

Declaration of Competing Interests

The authors declare that they have no known competing financial interest or personal relationships that could have appeared to influence the work reported in this paper.

Acknowledgements

The authors would like to acknowledge Queen Mary University of London and the Chinese Scholarship Council (Nos. 201806370199, 201706370217) for PhD scholarships to ZH and YY. The

authors are grateful to the Grant Agency of the Slovak Academy of Sciences (VEGA Grant No. 2/0038/20 and 2/0034/23), the National Natural Science Foundation of China (Nos. 12174164, 91963201 and 11834005) and the 111 Project under Grant No. B2006 for supporting this work. Dr Richard Whitely at Queen Mary University of London is thanked for his help in X-ray data collection.

References

[1] H. Schmid, Multi-ferroic magnetoelectrics, Ferroelectrics. 162 (1994) 317-338. https://doi.org/10.1080/00150199408245120.
[2] S. Dong, J.-M. Liu, S.-W. Cheong, Z. Ren, Multiferroic materials and magnetoelectric physics: symmetry, entanglement, excitation, and topology, Adv. Phys. 64 (2015) 519-626. https://doi.org/10.1080/00018732.2015.1114338.
[3] J. Wang, J.B. Neaton, H. Zheng, V. Nagarajan, S.B. Ogale, B. Liu, D. Viehland, V. Vaithyanathan, D.G. Schlom, U.V. Waghmare, N.A. Spaldin, K.M. Rabe, M. Wuttig, R. Ramesh, Epitaxial BiFeO3 multiferroic thin film heterostructures, Science. 299 (2003) 1719-1722. https://doi.org/10.1126/science.1080615.
[4] T. Kimura, T. Goto, H. Shintani, K. Ishizaka, T.-h. Arima, Y. Tokura, Magnetic control of ferroelectric polarization, Nature. 426 (2003) 55-58. https://doi.org/https://doi.org/10.1038/nature02018.
[5] N. Ikeda, H. Ohsumi, K. Ohwada, K. Ishii, T. Inami, K. Kakurai, Y. Murakami, K. Yoshii, S. Mori, Y. Horibe, H. Kito, Ferroelectricity from iron valence ordering in the charge-frustrated system LuFe2O4, Nature. 436 (2005) 1136-1138. https://doi.org/10.1038/nature04039.
[6] S. Ishiwata, Y. Taguchi, H. Murakawa, Y. Onose, Y. Tokura, Low-magnetic-field control of electric polarization vector in a helimagnet, Science. 319 (2008) 1643-1646. https://doi.org/10.1126/science.1154507.
[7] H. Khanduri, M. Chandra Dimri, H. Kooskora, I. Heinmaa, G. Viola, H. Ning, M. Reece, J. Krustok, R. Stern, Structural, dielectric, magnetic, and nuclear magnetic resonance studies of multiferroic Y-type hexaferrites, Journal of Applied Physics. 112 (2012) 073903. https://doi.org/10.1063/1.4754532.
[8] H. Murakawa, Y. Onose, S. Miyahara, N. Furukawa, Y. Tokura, Ferroelectricity Induced by Spin-Dependent Metal-Ligand Hybridization in Ba2CoGe2O7, Phys Rev Lett. 105 (2010) 137202. https://doi.org/10.1103/PhysRevLett.105.137202.
[9] A. Faraz, T. Maity, M. Schmidt, N. Deepak, S. Roy, M.E. Pemble, R.W. Whatmore, L. Keeney, Direct visualization of magnetic-field-induced magnetoelectric switching in multiferroic aurivillius phase thin films, Journal of the American Ceramic Society. 100 (2017) 975-987. https://doi.org/10.1111/jace.14597.
[10] L. Keeney, T. Maity, M. Schmidt, A. Amann, N. Deepak, N. Petkov, S. Roy, M.E. Pemble, R.W. Whatmore, Magnetic Field-Induced Ferroelectric Switching in Multiferroic Aurivillius Phase Thin Films at Room Temperature, Journal of the American Ceramic Society. 96 (2013) 2339-2357. https://doi.org/10.1111/jace.12467.
[11] P. Mandal, M.J. Pitcher, J. Alaria, H. Niu, P. Borisov, P. Stamenov, J.B. Claridge, M.J. Rosseinsky, Designing switchable polarization and magnetization at room temperature in an oxide, Nature. 525 (2015) 363-+. https://doi.org/10.1038/nature14881.
[12] D.M. Evans, A. Schilling, A. Kumar, D. Sanchez, N. Ortega, M. Arredondo, R.S. Katiyar, J.M. Gregg, J.F. Scott, Magnetic switching of ferroelectric domains at room temperature in multiferroic PZTFT, Nature Communications. 4 (2013). https://doi.org/10.1038/ncomms2548.
[13] K.Z. Rushchanskii, S. Kamba, V. Goian, P. Vanek, M. Savinov, J. Prokleska, D. Nuzhnyy, K. Knizek, F. Laufek, S. Eckel, S.K. Lamoreaux, A.O. Sushkov, M. Lezaic, N.A. Spaldin, A multiferroic material to search for the permanent electric dipole moment of the electron, Nature Materials. 9 (2010) 649-654. https://doi.org/10.1038/nmat2799.

[14] V. Koval, I. Skorvanek, J. Durisin, G. Viola, A. Kovalcikova, P. Svec, K. Saksl, H. Yan, Terbium-induced phase transitions and weak ferromagnetism in multiferroic bismuth ferrite ceramics, Journal of Materials Chemistry C. 5 (2017) 2669-2685. https://doi.org/10.1039/C6TC04060H.
[15] V. Koval, Y. Shi, I. Skorvanek, G. Viola, R. Bures, K. Saksl, P. Roupcova, M. Zhang, C. Jia, H. Yan, Cobalt-induced structural modulation in multiferroic Aurivillius-phase oxides, Journal of Materials Chemistry C. (2020). https://doi.org/10.1039/D0TC01443E.
[16] Z. Li, K. Tao, J. Ma, Z. Gao, V. Koval, C. Jiang, G. Viola, H. Zhang, A. Mahajan, J. Cao, Bi3.25La0.75Ti2.5Nb0.25(Fe0.5Co0.5)0.25O12, a single phase room temperature multiferroic, Journal of Materials Chemistry C. 6 (2018) 2733-2740. https://doi.org/10.1039/C8TC00161H.
[17] K. Tang, W. Bai, J. Liu, J. Yang, Y. Zhang, C.-g. Duan, X. Tang, J. Chu, The effect of Mn doping contents on the structural, dielectric and magnetic properties of multiferroic Bi5Ti3FeO15 Aurivillius ceramics, Ceramics International. 41 (2015) S185-S190. https://doi.org/10.1016/j.ceramint.2015.03.233.
[18] G. Kwei, A. Lawson, S. Billinge, S. Cheong, Structures of the ferroelectric phases of barium titanate, The Journal of Physical Chemistry. 97 (1993) 2368-2377. https://doi.org/10.1021/j100112a043.
[19] H.D. Megaw, Crystal structure of barium titanate, Nature. 155 (1945) 484-485. https://doi.org/10.1038/156177b0.
[20] B. Wul, Dielectric constants of some titanates, Nature. 156 (1945) 480-480. https://doi.org/10.1038/157297c0.
[21] H. Nakayama, H. Katayama-Yoshida, Theoretical prediction of magnetic properties of Ba(Ti1-xMx)O3 (M=Sc,V,Cr,Mn,Fe,Co,Ni,Cu), Japanese Journal of Applied Physics, Part 2: Letters. 40 (2001) L1355-L1358. https://doi.org/10.1143/jjap.40.l1355.
[22] S. Ray, P. Mahadevan, S. Mandal, S.R. Krishnakumar, C.S. Kuroda, T. Sasaki, T. Taniyama, M. Itoh, High temperature ferromagnetism in single crystalline dilute Fe-doped BaTiO3, Physical Review B. 77 (2008). https://doi.org/10.1103/PhysRevB.77.104416.
[23] S.G. Dhumal, A.N. Tarale, P.B. Joshi, D.J. Salunkhe, Structural, magnetic and magnetodielectric characteristics of Ni doped Ba0.95Sr0.05TiO3 single phase multiferroic compound, J Mater Sci-Mater El. 27 (2016) 5345-5350. https://doi.org/10.1007/s10854-016-4433-5.
[24] T.-L. Phan, P. Zhang, D. Grinting, S.C. Yu, N.X. Nghia, N.V. Dang, V.D. Lam, Influences of annealing temperature on structural characterization and magnetic properties of Mn-doped BaTiO3 ceramics, Journal of Applied Physics. 112 (2012) 013909. https://doi.org/10.1063/1.4733691.
[25] N.V. Dang, T.D. Thanh, L.V. Hong, V.D. Lam, T.-L. Phan, Structural, optical and magnetic properties of polycrystalline BaTi1−xFexO3 ceramics, Journal of Applied Physics. 110 (2011) 043914. https://doi.org/10.1063/1.3625235.
[26] N.V. Dang, P. The-Long, T.D. Thanh, V.D. Lam, L.V. Hong, Structural phase separation and optical and magnetic properties of BaTi1-xMnxO3 multiferroics, Journal of Applied Physics. 111 (2012). https://doi.org/10.1063/1.4725195.
[27] I.E. Grey, C. Li, L.M.D. Cranswick, R.S. Roth, T.A. Vanderah, Structure Analysis of the 6H–Ba(Ti, Fe3+, Fe4+)O3−δSolid Solution, Journal of Solid State Chemistry. 135 (1998) 312-321. https://doi.org/10.1006/jssc.1997.7652.
[28] R. Böttcher, H. Langhammer, T. Müller, H. Abicht, 3C–6H phase transition in BaTiO3 induced by Fe ions: an electron paramagnetic resonance study, Journal of Physics: Condensed Matter. 20 (2008) 505209. https://doi.org/10.1088/0953-8984/20/50/505209.
[29] P. Pal, K. Rudrapal, S. Mahana, S. Yadav, T. Paramanik, S. Mishra, K. Singh, G. Sheet, D. Topwal, A.R. Chaudhuri, Origin and tuning of room-temperature multiferroicity in Fe-doped BaTiO3, Physical Review B. 101 (2020) 064409. https://doi.org/10.1103/PhysRevB.101.064409.
[30] P. Pal, T. Paramanik, K. Rudrapal, S. Majumder, S. Yadav, S. Mahana, D. Topwal, R.J. Choudhary, K. Singh, A.R. Chaudhuri, Engineering room-temperature multiferroicity in Bi and Fe codoped BaTiO3, Applied Physics Letters. 117 (2020) 012901. https://doi.org/10.1063/5.0004785.
[31] G.-P. Du, Z.-J. Hu, Q.-F. Han, X.-M. Qin, W.-Z. Shi, Effects of niobium donor doping on the phase structures and magnetic properties of Fe-doped BaTiO3 ceramics, Journal of Alloys and Compounds. 492 (2010) L79-L81. https://doi.org/10.1016/j.jallcom.2009.12.031.

[32] S. Das, S. Ghara, P. Mahadevan, A. Sundaresan, J. Gopalakrishnan, D.D. Sarma, Designing a Lower Band Gap Bulk Ferroelectric Material with a Sizable Polarization at Room Temperature, ACS Energy Letters. 3 (2018) 1176-1182. https://doi.org/10.1021/acsenergylett.8b00492.
[33] Y. Yang, J.M. Liu, H.B. Huang, W.Q. Zou, P. Bao, Z.G. Liu, Magnetoelectric coupling in ferroelectromagnet Pb(Fe1⁄2Nb1⁄2)O3 single crystals, Physical Review B. 70 (2004) 132101-132104. https://doi.org/10.1103/PhysRevB.70.132101.
[34] A.C. Larson, R. Von Dreele, Program GSAS, General Structure Analysis System, Los Alamos National Laboratories, Los Alamos. (1994).
[35] B.H. Toby, EXPGUI, a graphical user interface for GSAS, Journal of Applied Crystallography. 34 (2001) 210-213. https://doi.org/10.1107/s0021889801002242.
[36] R. Buttner, E. Maslen, Structural parameters and electron difference density in BaTiO3, Acta Crystallographica Section B: Structural Science. 48 (1992) 764-769. https://doi.org/10.1107/S010876819200510X.
[37] R. Hesse, P. Streubel, R. Szargan, Product or sum: Comparative tests of Voigt, and product or sum of Gaussian and Lorentzian functions in the fitting of synthetic Voigt-based X-ray photoelectron spectra, Surface and Interface Analysis: An International Journal devoted to the development and application of techniques for the analysis of surfaces, interfaces and thin films. 39 (2007) 381-391. https://doi.org/doi.org/10.1002/sia.2527.
[38] G. Viola, T. Saunders, X. Wei, K.B. Chong, H. Luo, M.J. Reece, H. Yan, Contribution of piezoelectric effect, electrostriction and ferroelectric/ferroelastic switching to strain-electric field response of dielectrics, Journal of Advanced Dielectrics. 03 (2013). https://doi.org/10.1142/s2010135x13500070.
[39] W. Hamilton, Significance tests on the crystallographic R factor, Acta Crystallographica. 18 (1965) 502-510. https://doi.org/doi:10.1107/S0365110X65001081.
[40] R.D. Shannon, Revised effective ionic radii and systematic studies of interatomic distances in halides and chalcogenides, Acta Crystallographica section A: crystal physics, diffraction, theoretical and general crystallography. 32 (1976) 751-767. https://doi.org/10.1107/s0567739476001551.
[41] B. Luo, X. Wang, E. Tian, H. Song, Q. Zhao, Z. Cai, W. Feng, L. Li, Giant permittivity and low dielectric loss of Fe doped BaTiO3 ceramics: Experimental and first-principles calculations, Journal of the European Ceramic Society. 38 (2018) 1562-1568. https://doi.org/https://doi.org/10.1016/j.jeurceramsoc.2017.10.014.
[42] B. Yu, M. Li, J. Liu, D. Guo, L. Pei, X. Zhao, Effects of ion doping at different sites on electrical properties of multiferroic BiFeO3 ceramics, Journal of Physics D: Applied Physics. 41 (2008) 065003. https://doi.org/10.1088/0022-3727/41/6/065003.
[43] C. Yu, Y. Zeng, B. Yang, R. Wylde, R. Donnan, J. Wu, J. Xu, F. Gao, I. Abrahams, M. Reece, H. Yan, SrFe12O19 Based Ceramics with Ultra-low Dielectric Loss in the Millimetre-wave Band, Applied Physics Letters. 112 (2018). https://doi.org/10.1063/1.5022271.
[44] R. Sanjinés, H. Tang, H. Berger, F. Gozzo, G. Margaritondo, F. Lévy, Electronic Structure of Anatase TiO2 Oxide, Journal of Applied Physics. 75 (1994) 2945-2951. https://doi.org/10.1063/1.356190.
[45] M. Zubair, G. Li, B. Wang, L. Wang, H. Yu, Electrochemical Kinetics and Cycle Stability Improvement with Nb Doping for Lithium-Rich Layered Oxides, ACS Applied Energy Materials. 2 (2019) 503-512. https://doi.org/10.1021/acsaem.8b01534.
[46] B. Ravel, E. Stern, R. Vedrinskii, V. Kraizman, Local structure and the phase transitions of BaTiO3, Ferroelectrics. 206 (1998) 407-430. https://doi.org/10.1080/00150199808009173.
[47] Z. Chen, X. Bu, B. Ruan, J. Du, P. Zheng, L. Li, F. Wen, W. Bai, W. Wu, L. Zheng, Y. Zhang, Simultaneously achieving high energy storage density and efficiency under low electric field in BiFeO3-based lead-free relaxor ferroelectric ceramics, Journal of the European Ceramic Society. 40 (2020) 5450-5457. https://doi.org/https://doi.org/10.1016/j.jeurceramsoc.2020.06.073.
[48] J. li, J. Liu, M. Zeng, Z. He, H. Li, Y. Yuan, S. Zhang, High efficiency and power density relaxor ferroelectric Sr0.875Pb0.125TiO3-Bi(Mg0.5Zr0.5)O3 ceramics for pulsed power capacitors, Journal of the European Ceramic Society. 40 (2020) 2907-2916. https://doi.org/https://doi.org/10.1016/j.jeurceramsoc.2020.03.037.

[49] X. Liu, S. Xue, J. Ma, J. Zhai, B. Shen, F. Wang, X. Zhao, H. Yan, Electric-field-induced local distortion and large electrostrictive effects in lead-free NBT-based relaxor ferroelectrics, Journal of the European Ceramic Society. 38 (2018) 4631-4639. https://doi.org/https://doi.org/10.1016/j.jeurceramsoc.2018.06.023.
[50] A.A. Bokov, Y.H. Bing, W. Chen, Z.G. Ye, S.A. Bogatina, I.P. Raevski, S.I. Raevskaya, E.V. Sahkar, Empirical scaling of the dielectric permittivity peak in relaxor ferroelectrics, Phys Rev B. 68 (2003). https://doi.org/10.1103/PhysRevB.68.052102.
[51] A.K. Yadav, A. Anita, S. Kumar, A. Panchwanee, V.R. Reddy, P.M. Shirage, S. Biring, S. Sen, Structural and Ferroelectric Properties of Perovskite Pb(1−x)(K0.5Sm0.5)xTiO3 Ceramics, RSC Advances. 7 (2017) 39434-39442. https://doi.org/10.1039/c7ra07130b.
[52] Z. Zhao, V. Buscaglia, M. Viviani, M.T. Buscaglia, L. Mitoseriu, A. Testino, M. Nygren, M. Johnsson, P. Nanni, Grain-size effects on the ferroelectric behavior of dense nanocrystalline BaTiO 3 ceramics, Physical Review B. 70 (2004) 024107. https://doi.org/10.1103/PhysRevB.70.024107.
[53] Y. Tan, G. Viola, V. Koval, C. Yu, A. Mahajan, J. Zhang, H. Zhang, X. Zhou, N.V. Tarakina, H. Yan, On the origin of grain size effects in Ba (Ti0. 96Sn0. 04) O3 perovskite ceramics, Journal of the European Ceramic Society. 39 (2019) 2064-2075. https://doi.org/j.jeurceramsoc.2019.01.041.
[54] N. Maikhuri, A.K. Panwar, A.K. Jha, Investigation of A- and B-site Fe substituted BaTiO3 ceramics, Journal of Applied Physics. 113 (2013) 17D915. https://doi.org/10.1063/1.4796193.
[55] J.M. Coey, Magnetism and magnetic materials, Cambridge university press2010.
[56] F. Wan, X. Bai, K. Song, X. Han, J. Zheng, X. Lin, C. Cao, Effect of Co substitution on magnetic and magnetocaloric properties in multiferroic hexagonal YMnO3, Journal of Materials Science: Materials in Electronics. 28 (2017) 15819-15825. https://doi.org/10.1007/s10854-017-7476-3.
[57] J.B. Goodenough, Theory of the Role of Covalence in the Perovskite-Type Manganites [La, M(II)] MnO3, Physical Review. 100 (1955) 564-573. https://doi.org/10.1103/PhysRev.100.564.